J. Fluid Mech. (1968), *vol.* 34, *part* 1, *pp.* 91-111
Printed in Great Britain

Laboratory studies of wind-wave interactions

By JIN WU
HYDRONAUTICS, Incorporated, Laurel, Maryland

(Received 15 January 1968)

The present study consists of wind profile surveys, drift current measurements and water surface observations for a wide range of wind velocities in a wind-wave tank. It is confirmed that the velocity distribution essentially follows the logarithmic law near the water surface and the velocity-defect law toward the outer edge of the boundary layer. The wind stresses and surface roughnesses calculated from these distributions are divided into two groups separated by the occurrence of the wave-breaking phenomenon. For low wind velocities the surface roughness is dictated by ripples, and the wind-stress coefficient varies with $U_0^{-\frac{1}{2}}$, where U_0 is the free-stream wind velocity. The surface roughness is proportional to the average height of the basic gravity wave at higher wind velocities; the stress coefficient is then proportional to U_0. In addition, it is found that Charnock's expression ($k \propto u^{*2}/g$) holds only at high wind velocities, and that the constant of proportionality determined from the present experiment correlates very well with field observations. A new technique, involving the use of various-sized surface floats to determine the drift current gradient and the surface drift current, has been developed. A good agreement is shown between the gradients obtained from the measured currents and those determined from the wind stresses. Finally, the wind-stress coefficient is shown to be larger than the friction coefficient for turbulent flow along a solid rough surface; the difference is shown to be the wave drag of the wind over the water surface.

1. Introduction

It is generally considered that the turbulent air motion supports all the Reynolds stress, even quite close to the water surface, enabling us to adopt the shear velocity to characterize the wind field. Fragmentary measurements attempting to verify the logarithmic nature of the wind profile over water, have been conducted in the field and in laboratories by various investigators (Phillips 1966). There is, however, a lack of agreement among them and little or no correlation of their results with water surface conditions, which were unknown in most instances. In the present laboratory study, wind profiles under various wind conditions are systematically determined by the vertical traverse of a Pitot-static tube, and, simultaneously, the macro- and microscopic pictures of the disturbed water surface are recorded by a wave-height probe and a wave-slope gauge, respectively.

The present boundary-layer survey covering the inner- and outer-law ranges not only establishes the logarithmic distribution but also verifies the validity of the constants involved in this distribution (Schlichting 1960). This validity has previously been accepted without proof. The manner in which wind stress varies with wind velocities has been a controversy for many years. Part of this controversy may have resulted by comparison of data obtained in different wind-stress regimes whose existence is evident from the present study. A comparison of the difference between the wind stresses determined from the wind profile and those calculated for a solid surface covered by the equivalent roughness, and the measured magnitude of the wave building up along the wind direction, provides an evaluation of the wave drag.

Very few studies are available concerning the determination of the surface roughness which exerts a shearing stress upon the air; several widely different values of the surface roughness have been reported (Ursell 1956). Unfortunately, no attempt has been made to relate the surface roughness to wave observations, even though this must be considered a very fundamental step toward the understanding of wind–wave interactions. On the basis of a dimensional argument, Charnock (1955) suggested an equation of state relating the surface roughness to shear velocity; the implication of this argument attributes gravity waves to govern the surface roughness and leaves unnoticed the capillary waves. The present results have verified Charnock's expression (roughness governed by gravity waves), have suggested a new relationship for cases of capillary waves governing roughness, and have given evidence and explained the shift of the governing mechanism.

Due to the action of the wind stress, the existence of a strong drift current gradient below the air–water interface has long been realized. However, a single, finite-size particle has generally been adopted as the standard method for determining the surface drift current; consequently, the measurement depends undoubtedly on the float size. A new technique, using floats of various sizes in determining the drift current profile, has been employed. The extrapolation of the current profile to the water surface furnishes a better determination of the surface drift current and the stress calculated from the current profile is readily compared with that obtained from the wind stress. For the latter case, a detailed study may offer some indication of the energy transfer from wind to wave and also of the dissipation of wave energy.

2. Equipment and experimental procedure

2.1. *Wind–wave tank*

The principal part of the wind–wave tank is a flume with a 5 by 5 ft. cross-section 46 ft. long. The top of the tank is covered for 20 ft. up to the test section. Mounted at the upstream end of the tank is an axial flow fan, driven by a variable-speed motor. The maximum obtainable velocity with a 1 ft. deep air passage above the normal 4 ft. water depth is 45 ft./sec. A permeable-type wave absorber is installed at the downstream end, which effectively damps the short, high-frequency waves encountered in the present experiment.

2.2. *Wave measurement devices*

Ripples riding on top of gravity waves are typical of wind-generated waves, as shown in sample pictures of waves generated in the present tank (figure 1, plate 1), and make accurate measurement extremely difficult. A wave-height-measuring device is generally not accurate enough to register the ripple height, which is only a fraction of the basic gravity-wave height, and slope-measuring devices are awkward to use for the measurement of energy-containing waves. Consequently, two types of instruments have been used simultaneously in this experiment: a conductivity probe for recording gravity-wave heights and an optical instrument for counting ripple numbers. The former presents us with a macroscopic, and the latter a microscopic, picture of the wavy water surface under the blowing wind.

The conductivity probe is made of a 0·005 in. diameter partially submerged platinum wire acting as one electrode and a fully submerged aluminium plate as the other. The output depends on the electric current flow between the two electrodes, which in turn is proportional to the submergence of the wire. The optical instrument consists of a light source and a photomultiplier tube. The light focused on the water surface is reflected into the telescope (0·008 in. diameter view spot), which focuses an image of the water surface in front of the photomultiplier tube. The light source and the telescope are supported in a vertical plane; consequently the photomultiplier tube receives light signals only when a zero slope (of the water surface) is passing under the instrument. The outputs of both the conductivity probe and the optical instrument are recorded simultaneously on a visicorder. In addition, during some tests the signal of the conductivity probe was also fed continuously into an analogue computer to find the root-mean-square surface displacement.

2.3. *Velocity measurement devices*

Wind velocity measurement. The wind velocity profile in the tunnel is determined by the vertical traverse of a Pitot-static tube which is supported by a precise travelling mechanism. The test station is located at nearly equal distances from the two ends of the wave tank, where the mean water surface is believed to be least affected by the water surface set-up. However, the elevation of the tube above the water surface is corrected for the loss (by evaporation) of water from the tank during the test. The velocity head is registered by a zero-displacement-type micromanometer.

Drift current measurement. The drift current is measured by timing floats passing two stations at a fixed distance (about five basic wavelengths) apart along the tank. Spherical particles of various sizes (0·030, 0·125, 0·30 and 0·41 in. in diameter) and thin circular disks 0·1 in. in diameter and 0·022 in. thick are used as surface floats. The specific gravities of the floats are between 0·78 and 0·95. The velocity of the float is taken as the drift current at the location of the centroid of the submerged, projected area of the float. The velocity of the drift current is generally different from the phase velocity of the basic wave, and the float is seen climbing up and down the sloping water surface. However, according to

Francis (1956), the speed of the float in a sloping channel is essentially the same as the mean speed of the layer of the water in which the particle is floating.

3. Results

3.1. *Drift currents*

The distributions of the drift currents at different wind velocities are shown in figure 2; each point indicates the value averaged from more than 20 measurements. The drift current, v, is seen to decrease linearly with depth, at least for the part very close to the water surface. The gradients of the drift currents are shown as the slopes of the fitted straight lines. The indicated decrease of the gradient at the highest wind velocity is understandable since the mixing due to wave breaking might be expected to reduce the current gradient.

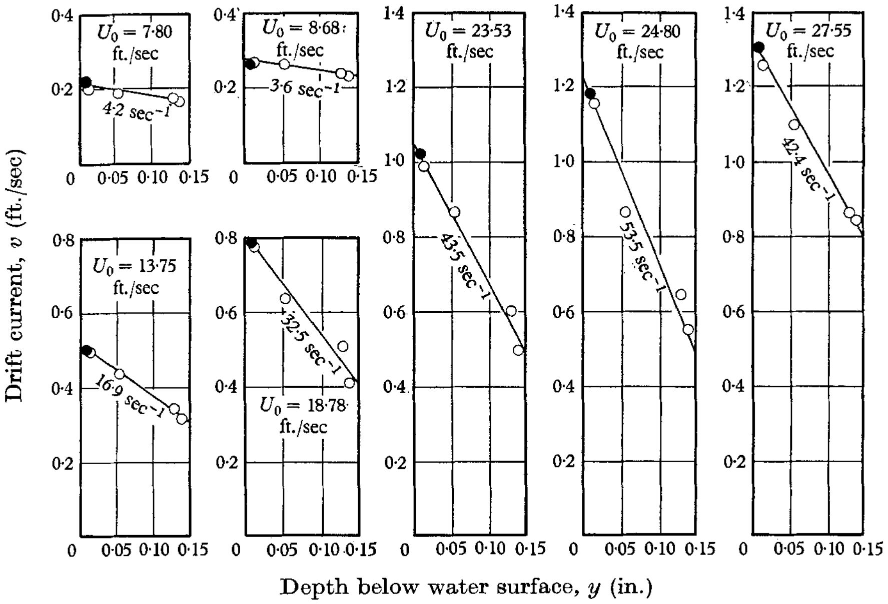

Figure 2. Gradients of drift currents. The data are obtained with: ●, circular disks; O, spherical floats.

The intersection of the fitted straight line with the water surface furnishes the value of the drift current, at the water surface, V. The surface drift currents as percentages of the measured wind velocities are plotted in figure 3. Besides showing that the percentage increases as the wind blows harder, the trend of the curve shows that an equilibrium stage (4·8 % of the free-stream wind velocity) is reached as the waves start to break. The same trend, this ratio approaching a constant value, was also reported by Keulegan (1951) (3·3 %). This is believed to be a more accurate technique of determining the surface drift current than is obtained by the conventional method of using particles of a single size and finite diameter, and explains why the present surface current is higher than those reported elsewhere.

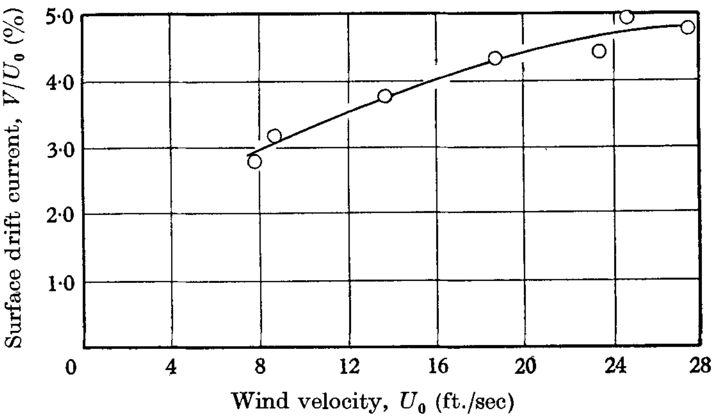

FIGURE 3. Drift currents and wind velocities. The experiment became especially difficult as the waves started to break at high wind velocity ($U_0 > 28$ ft./sec), since the breaking wave has a tendency to sink the surface float.

3.2. *Wind waves*

From the visicorder records, the periods and heights of more than 100 basic waves for each wind velocity are obtained. A period is the time interval for two successive wave troughs to pass the test station while the height is the average

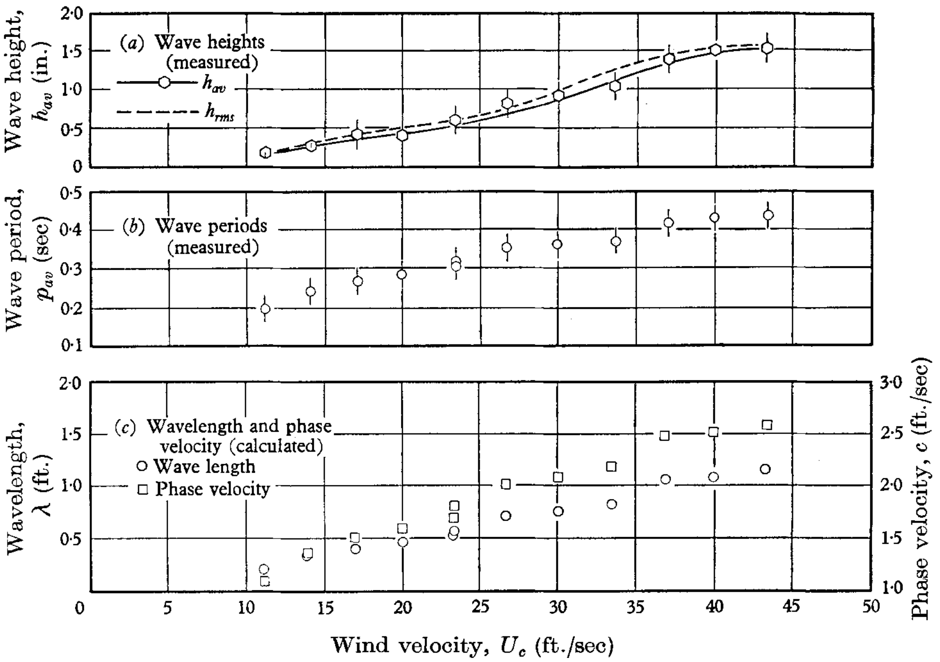

FIGURE 4. Wave periods, wave heights, wavelengths and phase velocities.

value of two vertical distances measured between the wave crest and its leading and trailing troughs, respectively. The average values of the wave periods, p_{av}, and wave heights, h_{av}, at various wind conditions are plotted in figure 4*a*, *b*, where U_c is the free-stream velocity relative to the water surface. For each wind velocity, a short vertical line representing the standard deviation of the data from the average value is also shown in the figure.

The root-mean-square and the average wave heights, plotted in figure 4*a*, are shown to change with wind velocity in a similar way. The rate of increase of wave height is small in the low-wind range; the wave generation by wind then becomes more effective and has its best efficiency at a wind velocity of $U_c \div 28$ ft./sec, when scattered whitecaps appear. An increase of the wind velocity above 40 ft./sec fails to result in further wave-height increase, as whitecaps are developed on every wave crest and as water particles are blown off the water surface, clearly indicating that the added energy is lost in wave breaking. It is also interesting to note that the tendency of an increase of wind velocity above 40 ft./sec to fail to obtain further effects is more pronounced for root-mean-square wave heights than average heights. Dominated more by the bigger waves which carry a larger component of total wave energy, the root-mean-square wave height is of course more closely related to the wave energy than is the average wave height.

Less than 20 % standard deviation is seen for the wave periods. The phase velocity, c, and wavelength, λ, of the typical waves are found from the wave periods, p_{av}, through several iterations between

$$c = \left\{\frac{g\lambda}{2\pi}\left[1+\left(\frac{\pi h_{av}}{\lambda}\right)^2\right]+\frac{2\pi\sigma}{\lambda\rho_w}\right\}^{\frac{1}{2}} \quad \text{and} \quad \lambda = c p_{av},$$

in which ρ_w is water density, g is gravitational acceleration, and σ is surface tension; see figure 4*c*. Both values are seen to increase almost linearly with the free-stream wind velocity. The average wavelength is always less than one-third of the water depth. Waves of the deep-water type are thus assured in the present experiment. In addition, the width of the wave channel is more than four times the wavelength; hence no side-wall effect on the development of the wind profile is expected.

The root-mean-square surface displacements, a_{rms}, determined through the continuous integration (on the analogue computer) of the output of a single conductivity probe placed at the test station, are plotted versus wind velocities in figure 5*a*. The rate of increase of the root-mean-square displacement, $\Delta a_{rms}/\Delta x$, shown in figure 5*b*, is obtained by applying the same technique to two probes, 3 ft. apart, placed at equal distances upwind and downwind from the test station and finding their simultaneous differences. The results show that the values of a_{rms} vary with wind velocity in a way similar to those of h_{rms} but with less pronounced variations, see figure 5*a*. As compared with the dashed line, $h_{rms}/2\sqrt{2}$ (corresponding to the surface displacement of a sinusoidal wave with height h_{rms}), the results also show that the waves are nearly sinusoidally shaped except when approaching the high-wind-velocity end as the waves start to break. As shown in figure 5*b*, the values of $(\Delta a_{rms}/\Delta x)/a_{rms}$ decrease with wind velocity initially as the phase velocity of the basic gravity waves also increases with wind velocity to make the fetch effectively shorter. The rate of increase of a_{rms} reverses its trend as the wave breaking halts wave development.

The number of light pulses per second, counted by the optical instrument is shown in figure 12. These pulses, corresponding to the numbers of crossings of the zero slopes for a randomly configurated water surface, are thus proportional to the number of ripples passing the test station. The pulses are seen first decreasing with an increase of wind velocity, reaching the minimum point just before the occurrence of wave breaking. The pulses then increase with wind velocity as waves start to break; and, finally, an equilibrium state is approached as whitecaps appear on almost every wave peak.

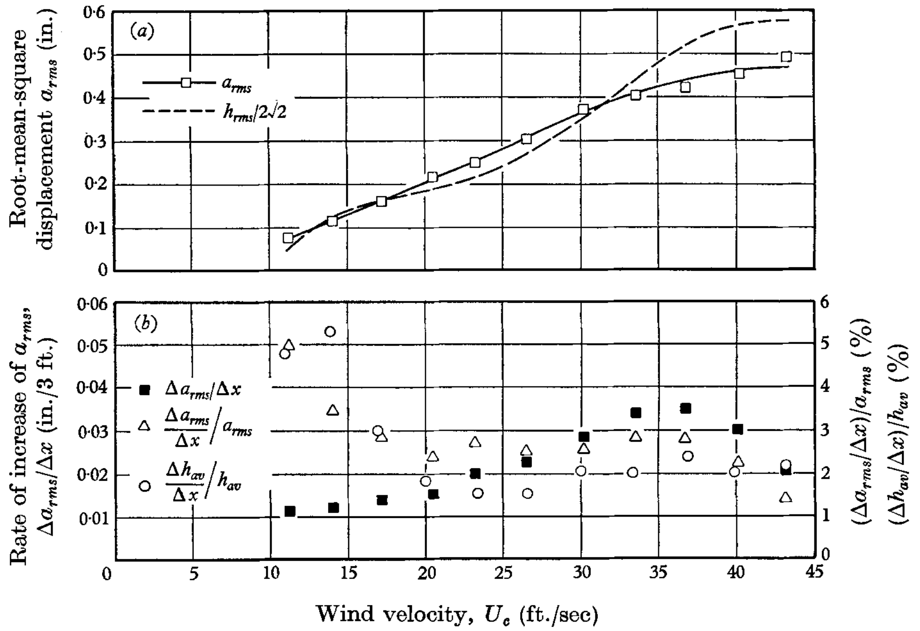

FIGURE 5. Root-mean-square surface displacements. More about $(\Delta a_{rms}/\Delta x)/a_{rms}$ and $(\Delta h_{av}/\Delta x)/h_{av}$ will be discussed in §4.2.

3.3. *Distribution of wind velocity*

Logarithmic law. The measured wind velocity, u, is plotted in figure 6 versus the distance above the mean water level, y. It is seen that a straight line can be drawn through a range of each wind profile compiled from the cases with various free-stream velocities. The free-stream velocity is determined from the middle flat part of the profile outside the boundary layers of both the cover plate and the water surface. Even at the lower end of the velocity profile, the wind velocities are between 6 and 14 times greater than the phase velocities of typical waves in each respective case. This indicates that the measurements are above the critical layer and inside the region of fully turbulent flow. This also offers an explanation as to why no kink on the measured velocity profile was observed.

The slopes of these straight lines, fitted through the experimental points, is proportional to the shear velocity, u^*. If the universal constant, 5·75, is assumed

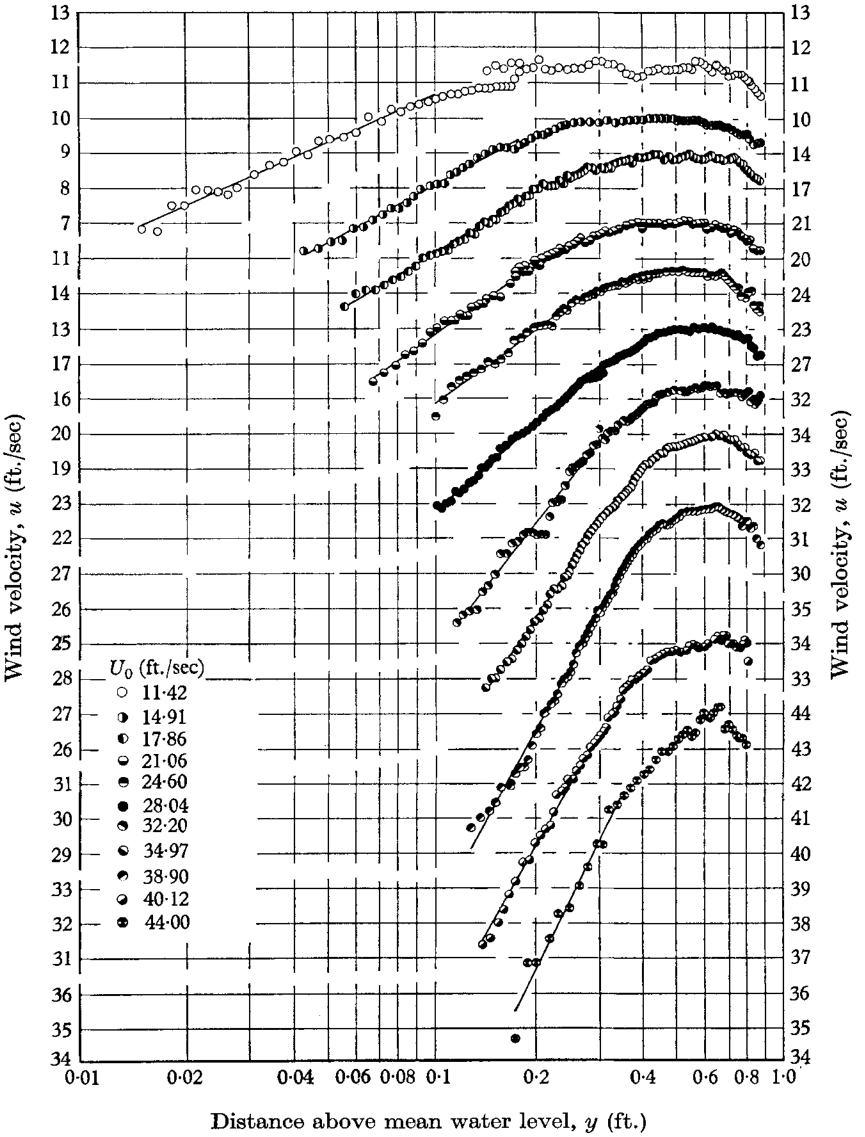

FIGURE 6. Vertical wind velocity distributions. The lower end of the logarithmic law region is nearly even with the maximum wave amplitude below which frequent wetting of the tube makes measurement impossible.

here, we can then calculate u^* from these slopes and write the inner law in the following dimensionless form (Schlichting 1960):

$$\frac{u}{u^*} = 5{\cdot}75 \log \frac{yu^*}{\nu} + A, \tag{3.1}$$

in which A is the intercept on the yu^*/ν axis.

However, the air–water interface is not stationary in this case, but moves in the wind direction at the velocity of the surface drift current. If we consider the wind velocities relative to the moving boundary, we have

$$\frac{u_c}{u^*} = 5{\cdot}75\log\frac{yu^*}{\nu} + B, \tag{3.2}$$

where u_c is the corrected wind velocity and B is a new intercept equal to 5·5 for a smooth boundary. Besides the surface drift current, each component of the water wave is moving in the wind direction with its own phase velocity. This makes the determination of the exact boundary condition extremely difficult. Some effects on the data analysis, due to the selection of the boundary condition, will be discussed in a later section.

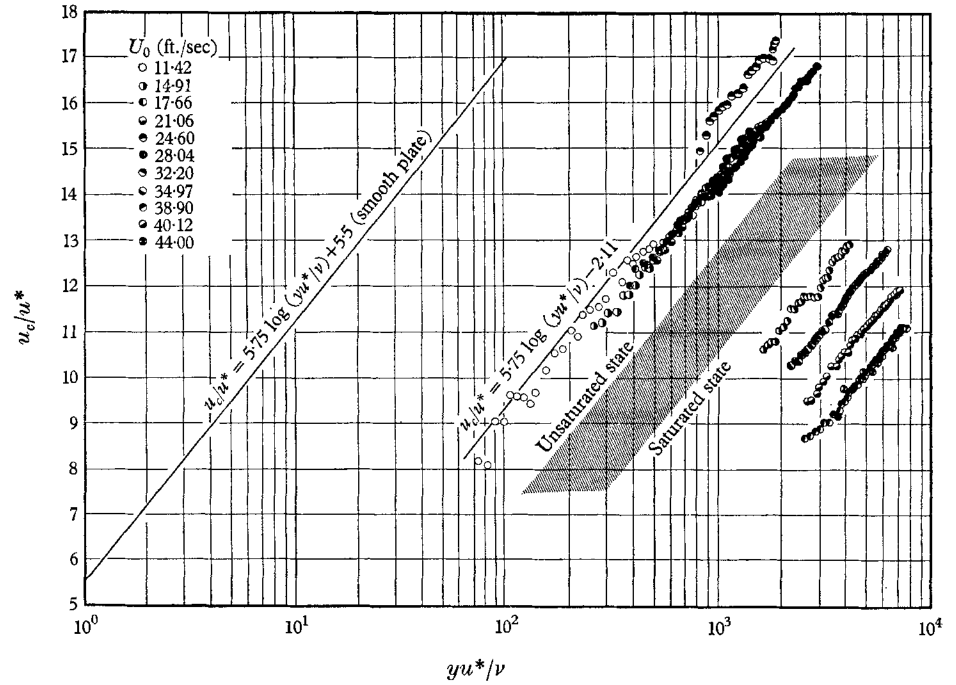

FIGURE 7. Wind velocity distributions. (Dimensionless plot.)

The corrected wind velocity data within the range of the logarithmic law are now plotted in dimensionless form in figure 7. The data are seen deviating from the smooth boundary expression; the farther the lines shift to the right, the more the flow becomes aerodynamically rough. It is known (Schlichting 1960) that the velocity distribution in the turbulent boundary layer over a completely rough surface is given by

$$\frac{u_c}{u^*} = 5{\cdot}75\log\frac{y}{k} + 8{\cdot}5, \tag{3.3}$$

in which k is a length scale characterizing the roughness of the water surface.

It is also known that $ku^*/\nu > 70$ corresponds to the aerodynamically rough flow regime. If we rewrite (3.3) in the form of (3.2) and substitute $ku^*/\nu = 70$ into the resulting equation, we find

$$\frac{u_c}{u^*} = 5{\cdot}75\log\frac{yu^*}{\nu} - 2{\cdot}11, \tag{3.4}$$

which is also plotted in figure 7. Near or to the right of the line, the flow condition is aerodynamically rough.

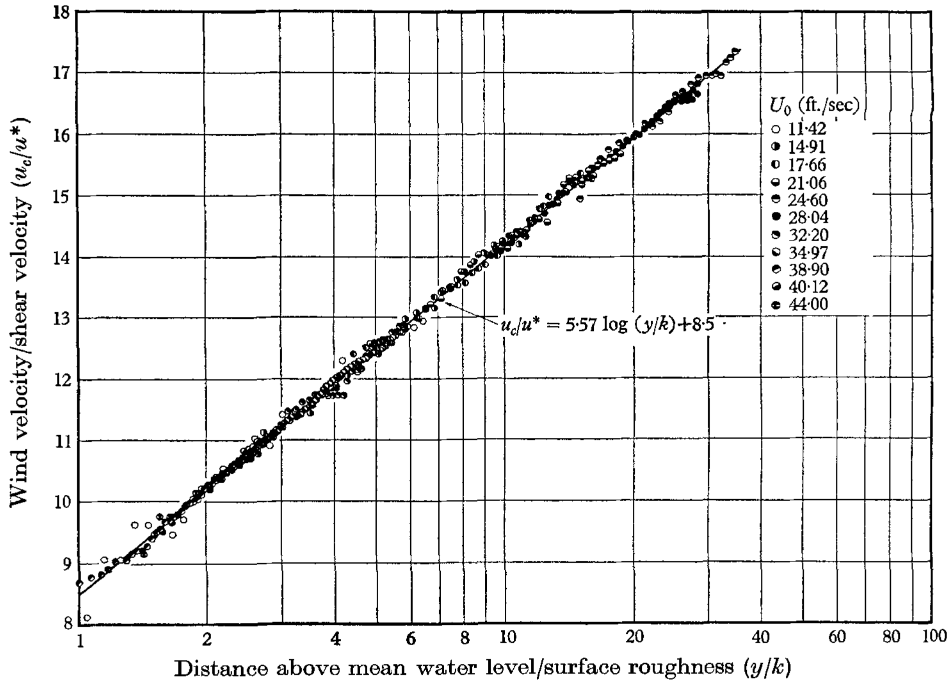

FIGURE 8. Logarithmic law of wind velocity distributions.

The data plotted in figure 7 are seen to be divided into two groups: one group, including those with low wind velocities, lies on the boundary of the completely rough flow regime; the second group, with high wind velocities, deviates widely from the first. These two groups are separated physically by the occurrence of wave breaking; that is, the wave is not saturated for the low-wind-velocity case and reaches the saturated state for the high-wind-velocity conditions. Since the flow is shown to be in the turbulent, rough regime for all cases except one, which is also in a nearly rough state, we can then choose the proper roughness scale suggested by (3.3) and replot the wind-velocity data in figure 8. The cluster of data compiled from various wind velocities is seen to correspond to the logarithmic velocity distribution law in the turbulent boundary layer along a rough surface.

Velocity-defect law (*outer law*). In the vicinity of the water surface, the wind velocity has been shown to follow the logarithmic law. It is interesting to see if the velocity-defect law, in the region overlapping the logarithmic law and extending to the outer edge of the boundary layer, can be well expressed by the parameters, shear velocity and roughness, derived from the logarithmic law.

The logarithmic law can be written in a general form as

$$u_c/u^* = f(y^*), \quad y^* = y/k, \tag{3.5}$$

while the velocity-defect law is expressed as

$$\frac{U_c - u_c}{u^*} = F(\zeta), \quad \zeta = \frac{y}{L}, \tag{3.6}$$

where L is a characteristic length (for which the ill-defined boundary-layer thickness is customarily adopted). Following Landweber & Siao's (1958) discussion for the turbulent boundary layer along a smooth surface, we find a natural and well-defined value for L, suggested by the boundary law for the rough surface.

Adding (3.5) and (3.6) and differentiating the sum with respect to y, we have for the overlapping range

$$y^* \frac{df}{dy^*} + \zeta \frac{dF}{d\zeta} = 0. \tag{3.7}$$

If we consider y^* and ζ as independent variables, then

$$y^* \frac{df}{dy^*} = -\zeta \frac{dF}{d\zeta} = a, \tag{3.8}$$

where a is a numerical constant. Following integration of (3.8) and the substitution of the numerical constants from (3.3), we have

$$U_c/u^* = f(y^*) + F(\zeta) = 5{\cdot}75 \log (L/k) + (8{\cdot}5 + b), \tag{3.9}$$

in which b is another numerical constant. If the length scale is so chosen to make $b = -8{\cdot}5$, we obtain

$$L = k \exp (U_c/2{\cdot}5u^*). \tag{3.10}$$

Therefore the velocity-defect law can be written as

$$\frac{U_c - u_c}{u^*} = -5{\cdot}75 \log \left[\frac{y}{k} \exp (-U_c/2{\cdot}5u^*)\right] - 8{\cdot}5. \tag{3.11}$$

The proper choice of the characteristic length scale, L, is reflected in the minimum scatter of the data plotted in the form suggested by (3.11), see figure 9. The straight line segment covers the inner–outer law overlapping range ending approximately at $(y/k) \exp (U_c/2{\cdot}5u^*) = 0{\cdot}025$ and is followed by a curve extending to the outside edge of the boundary layer as a cluster of data points approaches asymptotically the horizontal axis ($u_c = U_c$) as a limit.

The pattern of the data shown in figure 9 is quite meaningful because, during the process of data reduction, we first assume the universal constant (5·75) in the logarithmic law region to calculate u^* and then assume the Kármán–Prandtl velocity distribution in the same region to determine k. Based on these two parameters obtained previously, we are now able to correlate the wind data compiled from various wind velocities in the region extending to the outer edge of the boundary layer. This clearly confirms the application of the universal constant and the Kármán–Prandtl velocity distribution to wind blowing over a water surface. In other words, the structure of the turbulence and the consequent mean velocity profile not overly close to the water surface seems to be retained despite the water-induced air motion.

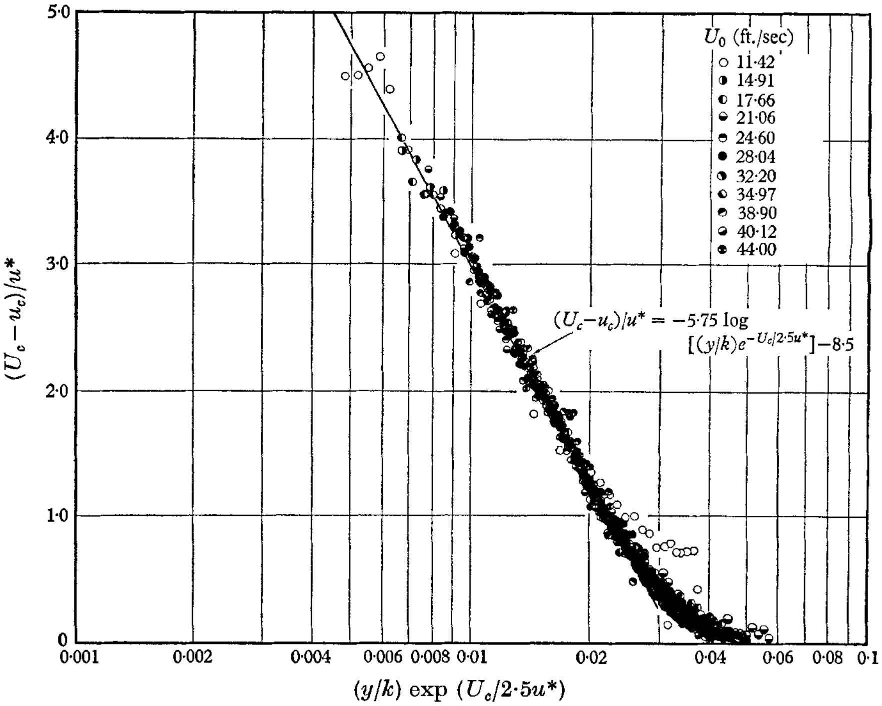

FIGURE 9. Velocity-defect law of wind velocity distributions.

4. Discussions

4.1. *Expressions relating shear velocity with surface roughness*

The results obtained from the logarithmic velocity law are plotted in figure 10*a*. The data are clearly divided into two groups: one previous to and the other subsequent to the occurrence of the wave-breaking phenomenon. Both shear velocity and roughness are seen to change linearly with the free-stream wind velocity in each respective group. The shear velocity increases more rapidly with the wind velocity in the second group than in the first. On the other hand, the roughness decreases before wave breaking and then increases as the wind speed increases beyond breaking.

It was first suggested by Charnock (1955), based on a dimensional argument, that for aerodynamically rough flow

$$\frac{k}{u^{*2}/g} = \text{constant}. \tag{4.1}$$

However, the present data, plotted in figure 10*b*, are found to support such an expression only at high wind velocities when, as will be shown later, the roughness is proportional to the average wave heights. This might have been anticipated since, as discussed subsequently, the wind stress at low wind velocities

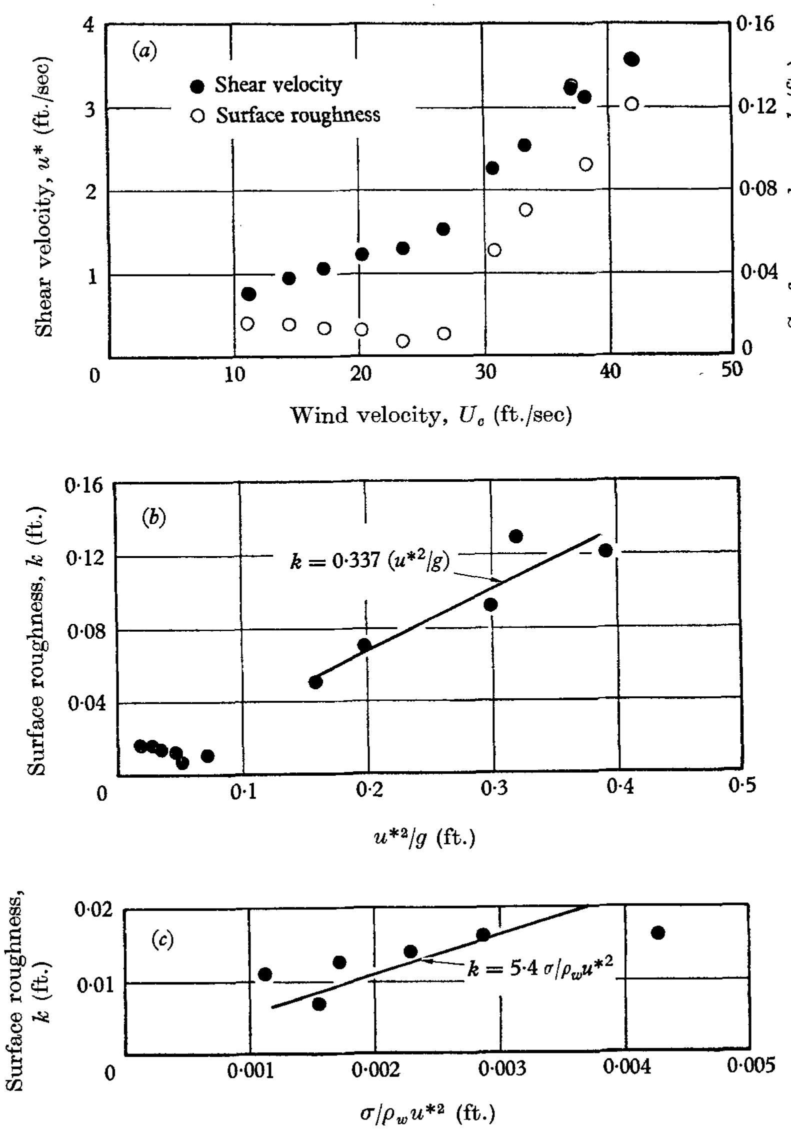

FIGURE 10. Shear velocity, surface roughness and expressions relating surface roughness to shear velocity.

is much more closely related to the steep-faced ripples (capillary waves) than to the gravity waves (which govern the average wave height), and, consequently, dimensionless parameters other than the one shown above may be formed. It is suggested that, since for the capillary waves the surface tension, σ, replaces gravity, g, as the parameter governing the wave motion, an alternative to (4.1), for conditions under which the capillaries alone determine the surface roughness, is given by

$$\frac{k}{\sigma/\rho_w u^{*2}} = \text{constant}. \tag{4.2}$$

Further study is required to determine accurately the proportionality constant for this new parameter when the roughness is dictated by the capillary waves. However, a tentative value (5.4) for this proportionality constant, based on the present data presented in figure 10*c*, is suggested.

4.2. *Wind stress*

The wind-stress coefficient calculated from shear velocity is plotted in figure 11. The results distinctly show the data to be divided once again by the occurrence of the wave breaking. As shown in figure 11, the stress coefficient changes with

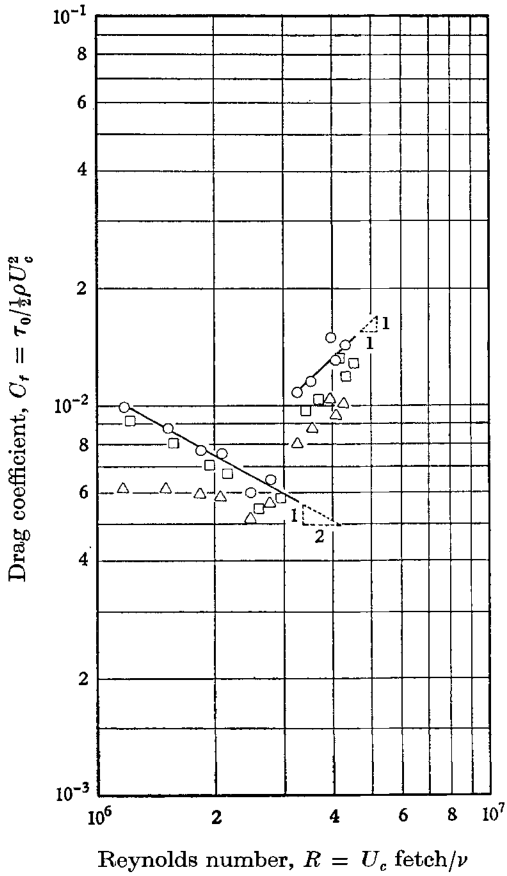

FIGURE 11. Wind-stress coefficients over water surface and friction coefficients along solid surface. Fetch is the distance between the fan section and the test station. R, Reynolds number (fetch); ○, calculated from shear velocity; □, calculated from shear velocity (without correction for drift current); △, solid boundary. $C_f = [2{\cdot}87 + 1{\cdot}58 \log (x/k)]^{-2{\cdot}5}$, k = calculated from wind velocity profile.

$U_c^{-\frac{1}{2}}$ (or $\tau_0 \sim U_c^{\frac{3}{2}}$) before the occurrence of wave breaking (unsaturated state). This implies that at this stage the stress coefficient decreases, and the water surface becomes aerodynamically smoother as the wind velocity increases. Opposite effects are shown in the wave-breaking stage (saturated state) since the stress coefficient increases linearly with the wind velocity (or $\tau_0 \sim U_c^3$). Slightly smaller values, but similar trends of variance with wind velocity, are shown for the wind-stress coefficient based on the measured wind velocity without the subtraction of surface drift current, see figure 11.

Assuming that the boundary layer is turbulent from the leading edge onwards, the coefficient of the local skin friction of a solid surface in the completely rough regime may be estimated from Schlichting (1960) to be

$$C_f = \{2{\cdot}87 + 1{\cdot}58 \log (x/k)\}^{-2{\cdot}5}, \tag{4.3}$$

where x is the distance downstream from the leading edge. By substituting the fetch and the local roughness obtained from the wind profile into (4.3), one can estimate the stress coefficient for the solid boundary with a corresponding roughness. This would certainly introduce a great error in calculating the mean friction coefficient, since the surface roughness upstream from the test station should be smaller than that measured at the test station. However, as far as the local friction coefficient is concerned, the effect may be secondary, as both the surface roughness and the boundary-layer thickness increase with the fetch. Therefore, the flow condition characterized by the ratio between the surface roughness and the boundary-layer thickness may not be altered to a large degree. So the estimated coefficient, plotted in figure 11, may be compared with the stress coefficient calculated from the wind velocity profile. The former is shown to be smaller than the latter in all cases; the larger difference shown at low wind velocities may be due to the fact that turbulent flow is not fully developed near the upstream end of the tank.

In contrast to the solid-surface condition, a portion of the drag exerted by the water surface on the wind is in the form of wave drag, which could also account for the difference discussed in the previous paragraph. This extra drag component is the rate of change of momentum transferred from the air to the wave by the interaction with the wavy water surface.

The wave momentum per unit area, M, can be approximated by the relationship for irrotational waves

$$M = \frac{E}{c} = \frac{\frac{1}{8}\rho_w g h_{av}^2}{[g\lambda_{av}/2\pi]^{\frac{1}{2}}}, \tag{4.4}$$

where E is the wave energy per unit area. The rate of change of momentum for wind waves (they reached an equilibrium stage at the test station but still built up with fetch) can be estimated from (4.4), and the wave-drag coefficient can be written, by assuming

$$\frac{d\lambda_{av}}{dx} = \frac{\lambda_{av}}{h_{av}}\frac{dh_{av}}{dx},$$

$$C_w = c\,\frac{dM}{dx}\bigg/\rho_a U_c^2 \doteqdot \tfrac{3}{16}\rho_w g h_{av}\,\frac{dh_{av}}{dx}\bigg/\rho_a U_c^2. \tag{4.5}$$

The wind-stress coefficients and the differences between wind-stress coefficients and friction coefficients of a solid surface are compiled in table 1. Let us consider, for the time being, these differences to be the wave drags. Except at low wind velocities, where the estimate of the friction coefficient of a solid surface from (4.5) is doubtful, and at high velocities, where the momentum loss due to the wave-dissipation mechanism (not included in the present estimate) is more pronounced, the average wave drag is about 20 % of the total wind stress. In fact, Stewart (1961), who first suggested that the wave drag is not negligible, also estimated that, based on field data, the wave drag has about this percentage of the total wind stress.

U_c (ft./sec)	Wind-stress coefficient $C_c \times 10^3$	Wave-drag coefficient $C_w \times 10^3$	C_w/C_c (%)	$\dfrac{dh_{av}}{dx}$ $C_w = 0{\cdot}2C_c$	$\dfrac{dh_{av}}{dx}\Big/h_{av}$ (ft.$^{-1}$)
11·03	9·97	3·80	38·1	0·0009	4·8
14·33	8·79	2·62	29·7	0·0012	5·2
17·11	7·73	1·75	22·7	0·0012	4·2
20·12	7·45	1·59	21·4	0·0012	3·0
23·45	6·05	0·91	15·0	0·0010	1·8
26·70	6·49	0·80	12·6	0·0010	1·5
30·65	10·82	2·72	25·2	0·0018	2·0
33·29	11·53	2·72	23·6	0·0019	1·9
37·03	14·98	4·60	30·7	0·0027	2·3
38·19	13·19	3·72	28·2	0·0024	2·0
41·89	14·34	4·16	29·1	0·0029	2·2

TABLE 1. Wave-drag coefficients

The rates of change of average wave height with fetch can then be estimated from (4.5) and plotted in figure 5*b*. Comparable percentages of rise are measured for the r.m.s. surface displacement. Moreover, similar trends are shown for both the estimated and the measured values. Therefore, it is confirmed that the wind stress can be obtained from the wind velocity profile and that the rather small difference between the wind stress and the friction calculated for a solid surface with the same roughness is mainly the wave drag.

4.3. *Surface roughness*

The water surface roughness calculated from the wind velocity profile will now be compared with measured wave conditions in an attempt to gain more physical insight about the significance of the calculated roughness. The roughness is thus plotted together with information about ripples in figure 12*a* and with basic wave data in figure 12*b*. It is revealed that, at lower wind velocities, the roughnesses show the same trend as the change of the light pulses per second with wind velocity, while, at higher wind velocities, the roughness correlates very well with the average basic wave heights.

The number of the light pulses is directly proportional to the number of ripples riding on basic gravity waves. The similar trend of variation with wind velocity between the pulses and roughness suggests that at this stage, before the occurrence of wave breaking, the basic gravity waves are flat-crested (see figure 9*a* and discussions) and the surface roughness is controlled by the ripples with steeper faces than the gravity waves. As the wind blows harder, the basic gravity waves become more and more sharp-crested; the ripples are no longer the dominant factor determining the surface roughness. The similar trend of variation and comparable magnitude between average wave height and roughness, at high wind velocity after the occurrence of wave breaking, indicates strongly that the wind stress is supported by the form drag of the basic gravity wave, and that flow separation likely occurs along the basic wave profile.

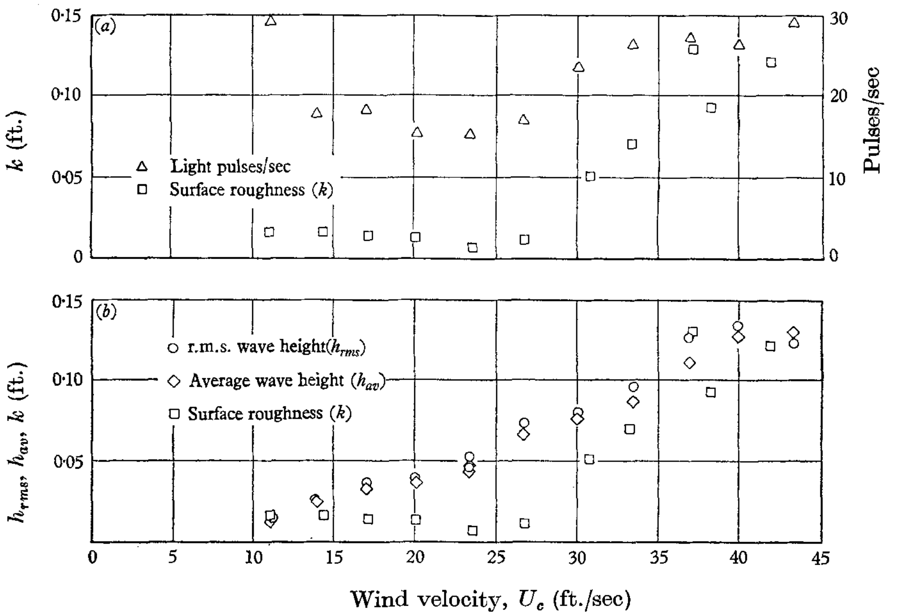

FIGURE 12. Roughness, number of capillary waves and average gravity-wave height.

It is worth while to note that at the lowest wind velocity, where the heights of the ripples are comparable to those of the gravity waves, the surface roughness has nearly the same magnitude as the average wave height, as might be expected.

The surface roughness discussed is calculated from the profile of wind velocity, which is obtained by subtracting the surface drift current from the measured wind velocity. It may be worth while at this point to compare these values of surface roughnesses with those obtained when some other velocity is used to correct the wind velocity, such as the phase velocity of the typical gravity wave, or when no correction is made. The surface roughness derived from these three different approaches is tabulated below. The same trends of change with wind velocity are shown for the surface roughness obtained by these three different methods. The roughnesses calculated on the basis of these two new approximations decreases more rapidly than the adopted approximation before the occurrence of wave breaking, but keeps the same ratio after breaking. In other words, the above-suggested correlation between the surface roughness and the wave conditions does not depend upon the precise way in which the wind data are analysed.

U_c (ft./sec.)	Corrected with drift current k (ft.)	Corrected with phase velocity k' (ft.)	k'/k	No corrections k'' (ft.)	k''/k
11·03	0·0160	0·0227	1·42	0·0131	0·82
14·33	0·0160	0·0222	1·38	0·0125	0·78
17·11	0·0138	0·0180	1·30	0·0104	0·75
20·12	0·0126	0·0155	1·23	0·0093	0·74
23·45	0·0069	0·0080	1·16	0·0048	0·70
26·70	0·0110	0·0131	1·19	0·0077	0·70
30·65	0·0503	0·0563	1·11	0·0383	0·76
33·29	0·0700	0·0766	1·09	0·0537	0·77
37·03	0·1292	0·1408	1·09	0·1023	0·79
38·19	0·0922	0·0995	1·08	0·0719	0·78
41·89	0·1204	0·1271	1·06	0·0949	0·79

TABLE 2. Surface roughness

4.4. *Gradients of drift currents*

The drift current indicated by the floats results from contributions both by the mean Eulerian velocity, as measured by a fixed probe, and by the mean Lagrangian velocity, $\bar{v}_l$. The latter is shown by Phillips (1966) to be

$$\bar{v}_l = \frac{2\pi\omega a^2 \cosh\left[4\pi(y+d)/\lambda\right]}{2\lambda \sinh^2(2\pi d/\lambda)}, \qquad (4.6)$$

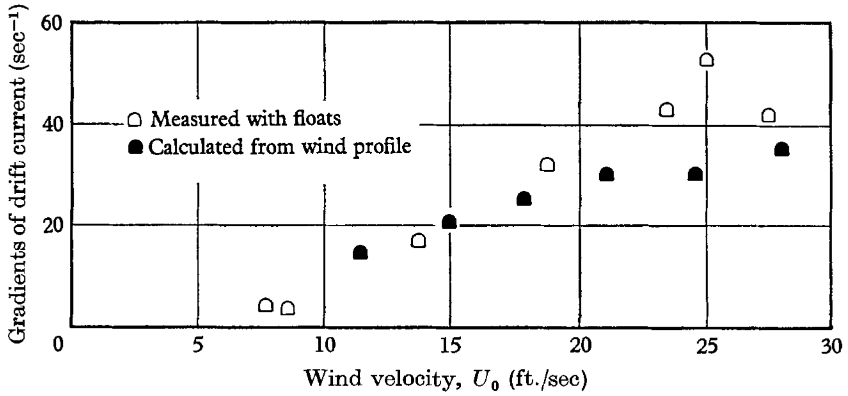

FIGURE 13. Gradients of drift currents.

where $\omega = 2\pi/p$ and d is the water depth; hence, at the water surface

$$(\bar{v}_l)_{y=0} = 4\pi^2 a^2/p\lambda \quad \text{as} \quad 2\pi d \gg \lambda.$$

This Lagrangian component is found generally to be only a fraction of the measured surface drift current, $(\bar{v}_l)_{y=0} = 0{\cdot}13\,V,$ and, since there is also uncertainty about the viscous effect on the foregoing expression, no correction has been made; the drift currents indicated by the floats were used for finding the wind velocities relative to the moving water surface.

By considering the continuation of the shear stress across the air–water interface, the Eulerian component of the drift current in the boundary layer can be calculated from (3.2). In order to compare these components with measured drift currents, calculations are made at the same distances below the mean water surface as those where the drift currents are measured. A straight line is then fitted through these calculated Eulerian components. The sums of these gradients indicated by the slopes of the straight lines and the gradients of the Lagrangian components, which can be found by differentiating $\bar{v}_l$ with respect to y, are plotted in figure 13. A good agreement is seen at lower wind velocities, and a fair comparison resulted for the higher wind velocities. The differences may well be due to the complicated flow structure very close to and on both sides of the air–water interface, as the interface becomes more disturbed by the wind; further studies are needed for a better understanding.

4.5. *Comparison of results with other works*

Many wind-stress measurements have been conducted in the laboratories by various investigators. The present results and those of other workers conducted in a laboratory tank are plotted in figure 14, in which the cross-sectional average

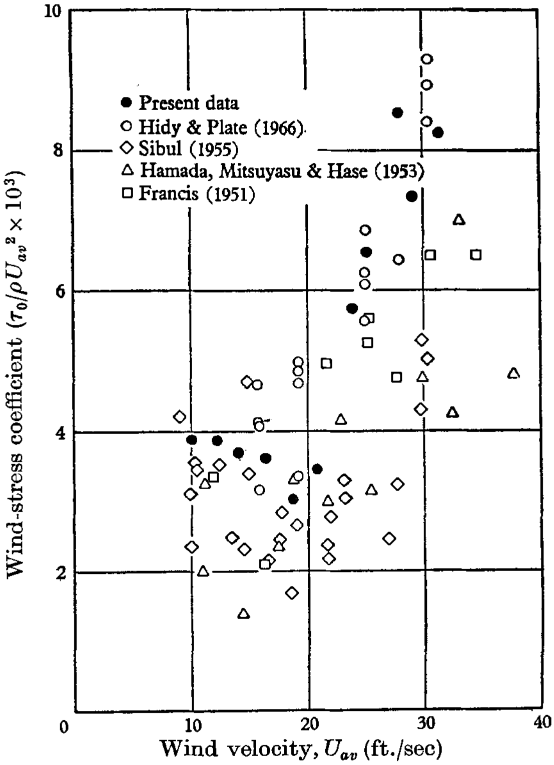

Figure 14. Comparison of results (wind-stress coefficients).

velocity is used. Instead of a linear relationship, a broken line trend, indicating that the stress coefficient increases more rapidly at high wind velocity than at low velocity, is seen for each set of data. The data from other works are scattered at the low wind velocities. However, the present least scattered result, having nearly the same magnitude as found by others, is seen to pass through the cluster of data points and clearly show the tendency of stress variation with wind velocity—the decrease of wind-stress coefficient with increase of wind velocity. At high wind velocities, good agreement is shown among the various works.

The present data support Charnock's expression at high wind velocities; the constant of proportionality is found to be 0·337, or 0·0112 if (3.3) and (4.1) are rewritten in the following forms:

$$\frac{u_c}{u^*} = 5{\cdot}75 \log \frac{y}{k_c} \quad \text{and} \quad \frac{k_c}{u^{*2}/g} = 0{\cdot}0112.$$

The same value (0·0112) appeared in part of the results reported recently by Hidy & Plate (1966). Moreover, following Phillips's (1966) argument this value is found to be consistent with the field observation. The value of 0·078 in Phillips's book was misprinted (private communication); in fact, the continuous line shown in figure 4.18 of Phillips (1966) corresponds almost exactly to the value 0·0112. This clearly indicates that under a steady wind where an equilibrium state between the wind profile and the water surface condition is reached at any given fetch, even though the shear velocity (or wind-stress coefficient) and the surface roughness (or average wave height) both depend very much on the fetch, the equilibrium state at any particular fetch can well be characterized by Charnock's expression (the only relationship between them on dimensional grounds). This further reveals the practicality of relating the laboratory wind-wave measurements with oceanic observations.

5. Conclusions

The present laboratory experiments consisted of wind profile surveys, water surface observations and drift current measurements for a wide range of wind velocities.

They confirm that the wind velocity distribution essentially follows the logarithmic law near the water surface, above the critical layer, and the velocity-defect law toward the outer edge of the boundary layer. The wind stress and the surface roughness calculated from these distributions indicate the existence of two distinct regimes separated by the occurrence of the wave-breaking phenomenon. In the first regime of unsaturated state, the surface roughness is shown to be dictated by the steeply faced ripples riding on basic gravity waves; the wind-stress coefficient varies with $U_c^{-\frac{1}{2}}$. For the saturated state of the second regime, the surface roughness is proportional to the average wave height, and the stress coefficient increases with U_c.

The present data are found to support Charnock's expression at high wind velocities when the roughness is proportional to the wave height. At low wind velocities when the wind stress is closely related to the capillary waves, a new expression involving the surface tension rather than gravity is suggested.

The wind-stress coefficient is found to be greater than the friction coefficient for turbulent flow along a solid surface with equivalent roughness. It is shown that the difference is mainly the wave drag of wind over the water surface.

A new technique has been developed, which involves the use of small floats of various sizes to determine the distribution of drift current and the extrapolation of the current profile to find the *surface* drift current. The present data show, as expected, that the current has a higher percentage of the wind velocity than other works using a single, finite-size float. A good agreement is shown between the gradient obtained from the measured currents and those derived from the wind stresses.

This study has been conducted to investigate the multiple adjustment of the wind profile and the water surface condition under an equilibrium state which is always reached between the wind and the waves for each steady wind velocity. Even though immediate applications of the present results to the field are not attempted, the data reveals the possibility of correlating laboratory and field studies by means of Charnock's expression.

I am indebted to Mr M. P. Tulin for his supervision of the work and review of this paper. I am also thankful to Prof. O. M. Phillips for the valuable discussion on several topics of this paper. I further acknowledge gratefully the co-operation of Mr W. van de Watering, Mr S. F. Wan and Mr J. Birkhead in carrying out part of the experiment. Most of the optical and electronic instrumentation used in this research was designed by Mr J. Lawrence. This work was supported by the Office of Naval Research, Department of the Navy, under Contract no. Nonr-3688(00).

REFERENCES

CHARNOCK, H. 1955 Wind stress on water surface. *Quart. J. Roy. Met. Soc.* **81,** 639.

FRANCIS, J. R. D. 1951 The aerodynamic drag of a free water surface. *Proc. Roy. Soc.* A **206,** 387.

FRANCIS, J. R. D. 1956 The speed of drifting bodies in a stream. *J. Fluid Mech.* **1,** 517.

HAMADA, T., MITSUYASU, H. & HASE, N. 1953 Experimental study of wind effects on water surface. *Transport Tech. Res. Rept. Tokyo,* no. 8.

HIDY, G. M. & PLATE, E. J. 1966 Wind action on water standing in a laboratory channel. *J. Fluid Mech.* **26,** 651.

KEULEGAN, G. H. 1951 Wind tides in small closed channels. *J. Res. Nat. Bur. Stand.* **46,** 358.

LANDWEBER, L. & SIAO, T. T. 1958 Comparison of two analyses of boundary-layer data on a flat plate. *J. Ship Res.* **1,** no. 4, 21.

PHILLIPS, O. M. 1966 *The Dynamics of the Upper Ocean.* Cambridge University Press.

SCHLICHTING, H. 1960 *Boundary Layer Theory.* New York: McGraw-Hill.

SIBUL, O. 1955 Laboratory study of the generation of wind waves in shallow water. *Beach Erosion Board Tech. Mem.* 72.

STEWART, R. W. 1961 The wave drag of wind over water. *J. Fluid Mech.* **10,** 189.

URSELL, F. 1956 *Wave Generation by Wind* in *Surveys in Mechanics* (ed. G. K. Batchelor and R. M. Davies). Cambridge University Press.

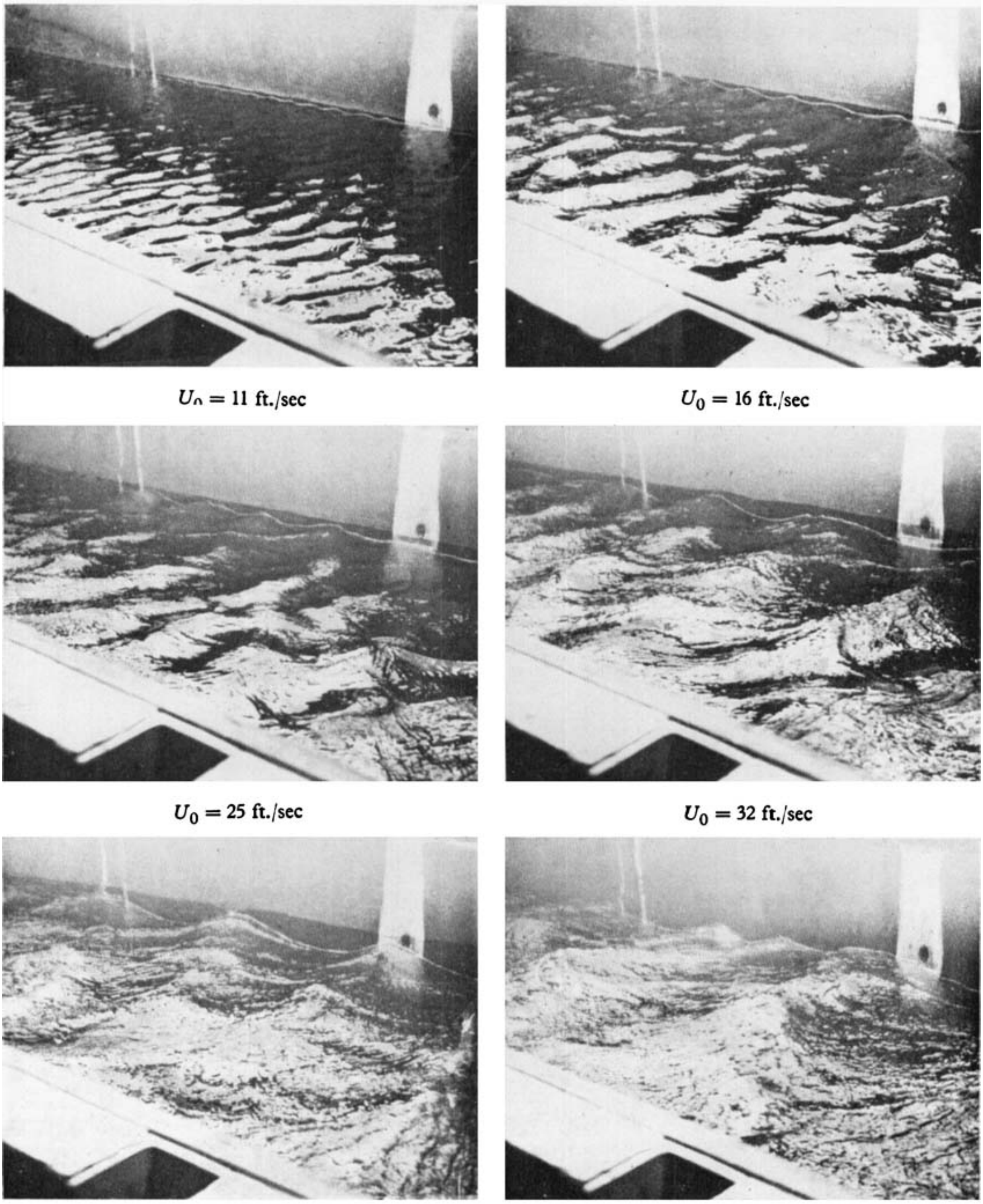

U_0 = 11 ft./sec

U_0 = 16 ft./sec

U_0 = 25 ft./sec

U_0 = 32 ft./sec

U_0 = 39 ft./sec

U_0 = 45 ft./sec

FIGURE 1. Sample pictures of wind waves generated in present tank.